Adjustable Inertial Response from the Converter with Adaptive Droop Control in DC Grids

Yi Wang, Member, IEEE, Chen Wang, Lie Xu, Senior Member, IEEE, Jianhui Meng, and Yang Hei

Abstract—In a DC grid, the inherent inertial support from the DC capacitors is too small to resist step changes or random fluctuations from the intermittent power resources, which results in lower DC voltage quality. In this paper, an adaptive droop control (ADC) strategy is proposed to achieve an increased inertia from the droop controlled converter. The adaptable droop coefficient according to the DC voltage variation enables fast swing of the droop curve, so that the converter can provide inertial power for the DC grid like synchronous generators in AC grids. The design of the ADC including the calculation and limitation of the adaptable droop coefficient is analyzed in detail. The small-signal analysis of the DC grid with ADC is provided to identify its stability issue. Experimental tests on a controller hardware-in-the-loop (HIL) platform of a low-voltage (LV) DC grid are carried out to validate the proposed method. In this LV DC grid, the proposed ADC is implemented on the energy storage system (ESS) which provides inertial support to improve the DC voltage quality under different power fluctuations, and smooths the power transmitted to AC grid.

Index Terms—DC grid, virtual inertia, voltage droop control, variable droop coefficient, adaptive control.

I. Introduction

DC grids are currently considered as creditable alternatives to AC grids for integrating renewable energy sources (RES) due to the distinct advantages, such as less power conversion and transmission loss, no concerns on reactive power consumption and power angle stability, and flexible power flow controllability [1]-[2]. However, the capacitance inertia of DC grids is far less than the mechanic inertia of conventional AC grids with synchronous generators [3]-[5]. During large disturbances, the abrupt change of the DC bus voltage may give rise to harmful impacts on sensitive loads and RES units. Moreover, step changes and random fluctuations from the intermittent generations can lead to drastic fluctuations of the DC bus voltage and power transmitted to AC grid. The voltage droop control is utilized on the converters in the DC grid to ensure its voltage stability by redistributing power automatically during disturbances [6]-[7]. However, the output power of the converter has to approach a new operating point by following the droop curve during disturbances. Thus, it cannot mitigate the mutation rate of the DC voltage effectively due to the distinct power unbalance on the capacitor exits. Therefore, introducing virtual inertia control to the DC grid is necessary to improve its voltage quality.

The AC grid with high penetration rate of RES is also a low-inertia system [8]-[9]. To resolve this problem, virtual inertia control methods arouse great attention in recent years. The concept of virtual synchronous machines (VSM) is proposed in [10] and the moment of inertia in synchronous machines can be emulated by the converters of RES. In [11] and [12], inverters named synchronverters are controlled to behave in the same way as synchronous generators to ensure smooth transition of inverter dominated grids. In [13], an optimized power point tracking (OPPT) controller is proposed to shift the operating point of a permanent magnet synchronous generator (PMSG)-based wind turbine from the MPPT curve to the virtual inertia control curve according to the frequency deviation.

In DC grids, the DC capacitors store energy and create a kind of inertia for DC voltage to resist its rapid change. However, the equivalent inertia of the capacitors is far less than that of the rotating mass of a synchronous generator with similar VA rating. Therefore, the DC grid is a small inertia system and its DC voltage can vary rapidly during power imbalance. The virtual inertia control can be introduced to the DC grid to prevent fast DC voltage transient, though there has been limited research on the topic. In [14], an ultra-capacitor is added to offer a transient compensation when a sudden load is switched on and therefore the transient response is improved. However, the ultra-capacitor has high cost and remains idle when the DC grid is under steady-state operation, which makes it unproductive. To avoid the over-charging and over-discharging conditions for the energy storage system (ESS), virtual inertia control is proposed for the RES units in a DC grid [15]. However, it mainly focuses on the coordinated control among micro-sources with little details on the analysis of the virtual inertia control. In [16], the DC bus voltage is introduced to the speed regulation of PMSG-based wind turbines and a virtual inertia control strategy for the wind-battery-based islanded DC microgrid is proposed. The rotational kinetic energy of the wind turbines is utilized to supply virtual inertia, but it is not suitable for other kind of RES such as the PV generation. In [17], a virtual inertia control strategy analogized with VSM is presented to enhance the inertia of the DC microgrid. However, an auxiliary control loop to emulate VSM characteristic has to be added in the converter control system. Therefore, for droop controlled converters in DC grids, the coordination between supplemental inertial control and primary voltage regulation needs to be considered.

Voltage droop control is regarded as a practical scheme for power sharing in DC grids [18]-[21]. Some modified droop

This work was supported by the National Key R&D Program of China under Grants 2016YFB0900203.

Y. Wang, C. Wang, J. Meng and Y. Hei are with the State Key Laboratory of Alternate Electrical Power System with Renewable Energy Sources, North China Electric Power University, Baoding 071003, China (e-mail: yi.wang@ncepu.edu.cn).

L. Xu is with the Dept. of Electronic & Electrical Engineering, University of Strathclyde, Glasgow, UK.

controllers have been presented recently to further enhance the voltage quality and stability of DC grids [22-27]. In [22], an improved decentralized DC power management strategy based on P-V_{dc}^2 droop is designed to enhance the dynamics of DC power regulation. In [23], a droop controller suitable for multi-time scale power control is presented to realize proper power interaction among different sub-grids. In [24], the relationship between AC frequency and DC voltage identified via the interactive virtual inertia and capacitance is used to design the voltage control strategy for AC/DC interface for improving the system stability. In [25], an observer-based DC voltage droop and a current feed-forward control for a DC microgrid are proposed to improve the dynamic response of DC voltage control. Although abovementioned control schemes can improve the dynamic performances of DC grids, the controller designs tend to be more complicated than the conventional droop control, due to the fact that modified control for dynamics improvement may be coupled with the primary voltage regulation and power sharing.

This paper proposes a control method to combine the virtual inertia control with the voltage droop control to increase the inertia of DC grids without additional controllers. The proposed adaptive droop control (ADC) will initially utilize a fast swing of the droop curve to emulate inertial response as a virtual capacitance during disturbances, whereas the droop curve will resume fixed as the DC voltage approaches to a steady state. Thus, the swing of the droop curve only takes effect to suppress the voltage mutation at the initial stage of disturbances, and has little effect on the subsequent primary voltage regulation and power sharing. Therefore, the inertial response obtained by this way can be more easily integrated with the conventional droop control. This paper is organized as follows. Section II illustrates the DC grid under investigation and gives the principle of the voltage droop control. Detailed inertia analysis of the DC grid is described in Section III, and the study of the virtual inertia control based on the variable droop coefficient is carried out. By modifying the variable droop coefficient, an adaptive droop control strategy with inertial response is proposed in Section IV. Section V investigates the stability issue of the DC grid with ADC using small-signal analysis. Experimental results based on a hardware-in-the-loop (HIL) platform of a low-voltage (LV) DC grid are presented in Section VI to validate the proposed control strategy. Finally, conclusions are drawn in Section VII.

II. DC Grid Configuration and Control

A. Configuration of the DC Grid for RES Integration

A typical configuration of the DC grid for RES integration is shown in Fig. 1, where four different kinds of terminals are connected to the DC grid by converters, i.e. RES, AC/DC loads, AC grid and energy storage system (ESS). The DC transformers (DC-DC converter), namely P-DCT and W-DCT, are used to connect the PV units and wind turbines to the DC grid, respectively. AC loads are connected to the DC bus via a DC-AC converter L-VSC, while DC loads can be connected to the DC bus directly or via a DC transformer L-DCT. The G-VSC connects the DC grid to the AC grid. The ESS of a DC grid can be based on batteries, super capacitors, flywheels, etc. Battery energy storage system (BESS) is most commonly used and is discussed in this paper. The BESS is connected to the DC bus via a bidirectional DC transformer E-DCT.

The RES units and loads usually operate on their own merits and do not actively contribute to system control. The G-VSC and BESS are responsible for balancing the power surplus/deficit caused by RES units and loads and ensuring stable operation of the system. In this paper, voltage droop control is adopted as the primary voltage regulation strategy for the DC grid to coordinate the G-VSC and E-DCT (BESS).

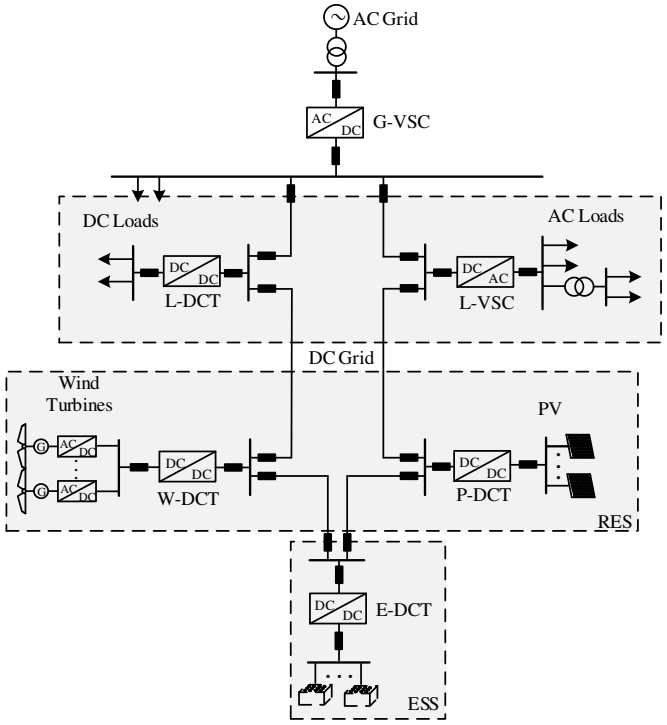

Fig. 1. Typical configuration of a DC grid for RES integration.

B. Voltage Droop Control

One of the classical decentralized power management methods is the voltage-power (V-P) droop control, in which the deviation of the DC bus voltage is used for autonomous power sharing among different sources. The characteristics of V-P droop control are shown in Fig. 2, which can be expressed as

$$V_{dc} = V_{dc}^{*} - \frac{1}{k}(P - P^{*}) \tag{1}$$

where V_{dc} and P are the DC bus voltage and output active power of the converter respectively. The superscript * refers to the reference values, and k is the droop coefficient.

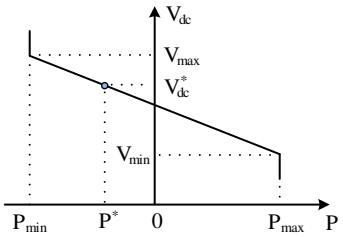

Fig. 2. Characteristics of V-P droop control.

III. Principle of Adaptive Droop Control with Adjustable Inertia

For a DC grid using droop control, only capacitors directly contribute to the resistance of the voltage change rate dV_{dc}/dt. This can lead to the deterioration of DC voltage quality, such as

voltage flicker and higher-frequency fluctuations. In this section, DC grid inertia is introduced and detailed analysis of the controllable inertia of the DC grid based on adaptive droop control is described in order to reduce the transient DC voltage variation.

A. DC Grid Inertia Definition

For an AC power system, inertia reflects the system capability in preventing the frequency from a sudden change. Due to the existence of inertia, generators have sufficient time to adjust their generated power and reestablish the power balance. The inertia time constant H_s of a traditional synchronous generator can be defined as

$$H_s = \frac{W_k}{S_N} \tag{2}$$

where W_k is the kinetic energy stored in the rotor at rated rotating speed and S_N is the nominal generation capacity.

The definition of the DC grid inertia can be developed from the same concept of the AC system, i.e. DC power system inertia reflects the system capability in preventing the DC voltage from a sudden change. Generalizing (2) to DC systems, the inertia time constant H_{dc} of one terminal of the DC grid can be defined as

$$H_{dc} = \frac{W_e}{S_{Nc}} = \frac{C}{2}\frac{V_N^2}{S_{Nc}} \tag{3}$$

where W_e and S_{Nc} refer to the stored capacitor energy at nominal DC voltage V_N and nominal capacity, respectively. C is the capacitance value of a DC terminal. The physical meaning of H_{dc} can be described as the amount of time required to release all the electric energy stored in the capacitor at the rate of S_{Nc}. Therefore, the larger C is, the larger H_{dc} and DC grid inertia are.

For a synchronous generator, the typical value of H_s is approximately a few seconds. For a DC terminal, according to (3) and assuming the rated V_N and S_{Nc} of 10kV and 4MW, a capacitor with a few tenth of farad is required to make H_{dc} possess the same magnitude order as H_s. However, the required C value is much larger than that of a typical DC capacitor in such a system.

B. Principle of Virtual Inertia in DC Grid

The equivalent circuit of a converter in DC grids is shown in Fig. 3(a), where P_R represents the total power by the RES units and loads, and P_S represents the power supplied by a power source such as the BESS. The power relationship of the circuit in Fig. 3(a) can be expressed as

$$P_S - P_R = CV_{dc}\frac{dV_{dc}}{dt}. \tag{4}$$

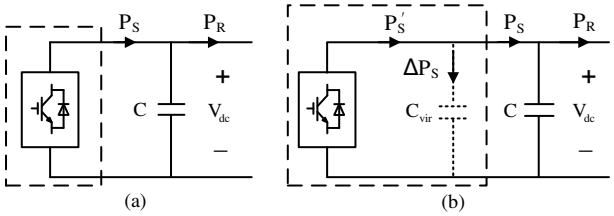

Fig. 3. Equivalent circuit of a converter in DC grids. (a) Without virtual inertia control. (b) With virtual inertia control.

It can be inferred from (4) that a constant DC voltage indicates a balanced power flow. During system disturbances such as power fluctuations by the RES units and/or loads, the larger C is, the smaller dV_{dc}/dt becomes. However, as analyzed above, the DC capacitance value is small in practice.

In order to increase the equivalent inertia of a DC system, virtual inertia control is adopted and is implemented on the converters. As shown in Fig. 3(b), the auxiliary power ΔP_S is supplied to slow down the voltage change rate during the variation of DC bus voltage as given by

$$\Delta P_S = C_{vir}V_{dc}\frac{dV_{dc}}{dt} \tag{5}$$

where C_{vir} is the equivalent capacitance added by virtual inertia control in the DC side of the converter, referred to as the virtual capacitance. Taking ΔP_S into account, the supplied power can be updated as

$$P_S = P_S' - \Delta P_S \tag{6}$$

where P_S' is the supplied power without virtual inertia control.

Substituting (5) and (6) into (4) yields

$$(C + C_{vir})V_{dc}\frac{dV_{dc}}{dt} = P_S' - P_R. \tag{7}$$

Equation (7) indicates that during the variation of V_{dc}, the equivalent DC capacitance is enlarged because of C_{vir} by the virtual inertia control. According to (3) and taking C_{vir} into account, H_{dc} can be modified as

$$H_{dc} = \frac{C + C_{vir}}{2}\frac{V_N^2}{S_{Nc}}. \tag{8}$$

From (8), it can be seen that with the virtual inertia control, the inertia of the DC grid is increased and a reduced dV_{dc}/dt can be obtained.

C. Virtual Inertial Response by Swing of Droop Curve

The auxiliary power mentioned above can be supplied quickly by swinging the voltage droop curve and the dynamic swing of the droop curve can be realized by changing the droop coefficient. Figs. 4 (a) and (b) show the relevant schematic diagrams for positive (supply) and negative (absorb) power directions, respectively, where O is the reference point (P^* is normally taken as 0) and A is the steady state operating point on the droop curve ①. V_A and P_A refer to the corresponding DC voltage and active power of point A, respectively. Under steady state, $P_R = P_S = P_A$.

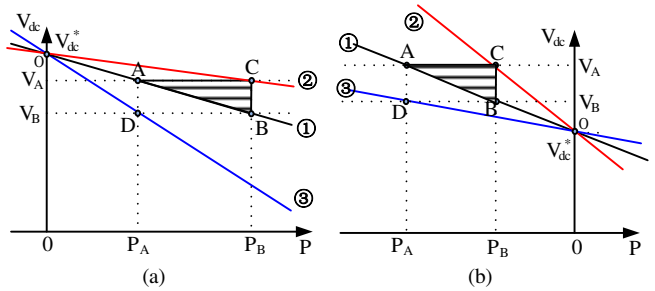

Fig. 4. Schematic diagram of virtual inertial response by swing of droop control curve. (a)P>0. (b)P<0.

When P_R suddenly increased from P_A to P_B, the unbalanced power between P_R and P_S during this transient process causes a rapid decline of the capacitor voltage (i.e. $dV_{dc}/dt<0$). The operating point of the converter will move from A to B along the curve ① to increase its power output from P_A to P_B under

the normal droop control. The power difference between P_R and P_S during this transient process will be reduced from P_B-P_A to 0 along the curve AB gradually. To provide virtual inertia response, if P>0, the droop curve quickly swings anti-clockwise form ① to ② by increasing the droop coefficient k, as shown in Fig. 4(a). If P<0, curve ① swings clockwise to curve ② by decreasing k, as shown in Fig. 4(b). Thus, the converter can immediately release power from P_A to P_B without large DC voltage drop. When a suddenly reduction of P_R from P_B to P_A occurs (i.e. $dV_{dc}/dt>0$), curve ① swings clockwise/anti-clockwise to curve ③ by decreasing/increasing k and at the same time, the converter can absorb the power quickly to slow down the change rate of the capacitor voltage.

According to the above analysis, the fast swing of the droop control curve can make the converter release/absorb power more quickly than the fixed droop curve, so as to achieve the inertial response of resisting the voltage change rate. The variable droop coefficient k can be associated with dV_{dc}/dt and is defined as

$$k = K_1 + \mathrm{sign}(V_{dc} - V_{dc}^*)\cdot K_2 \frac{dV_{dc}}{dt} = K_1 + K_2^{'}\frac{dV_{dc}}{dt} \quad (9)$$

$$K_2^{'} = \mathrm{sign}(V_{dc} - V_{dc}^*)\cdot K_2 \quad (10)$$

where K_1 is the droop coefficient under steady state. K_2 is the virtual inertia coefficient, and $K_2>0$.

As seen in (9) and (10), k is proportional to dV_{dc}/dt and the sign symbol of $K_2^{'}$ is determined by the position relationship between the operating point and the reference point. Under steady state, dV_{dc}/dt is equal to zero and k remains constant at K_1. Once V_{dc} varies due to power disturbances, k increases or decreases and the droop curve swings to offer auxiliary power to enhance the inertia of the DC system. For purpose of preventing the absorbed power from exceeding the maximum value, swing range of the droop curve should be limited between the lower limit K_{min} and the upper limit K_{max}.

In order to estimate the virtual inertia supplied by virtual inertia control based on the variable droop coefficient given in (9), the virtual capacitance C_{vir} is deduced here.

Substituting (9) into (1) and according to (6), P_S is obtained as

$$\begin{aligned} P_S &= K_1(V_{dc}^* - V_{dc}) + K_2^{'}(V_{dc}^* - V_{dc})\frac{dV_{dc}}{dt} \\ &= P_S^{'} + K_2^{'}(V_{dc}^* - V_{dc})\frac{dV_{dc}}{dt} \end{aligned}. \quad (11)$$

Substituting (11) into (4) yields

$$CV_{dc}\frac{dV_{dc}}{dt} + K_2^{'}(V_{dc} - V_{dc}^*)\frac{dV_{dc}}{dt} = P_S^{'} - P_R . \quad (12)$$

Comparing (12) with (7), C_{vir} can be obtained as

$$C_{vir} = K_2^{'}\left(\frac{V_{dc} - V_{dc}^*}{V_{dc}}\right) = K_2\frac{|V_{dc} - V_{dc}^*|}{V_{dc}}. \quad (13)$$

Equation (13) reveals that C_{vir} varies with V_{dc} and is controllable by adjusting K_2. Thus, the virtual inertia emulated by the adaptive droop control is not fixed, and it can be adjusted as required. The larger K_2 is, the larger C_{vir} and supplied virtual inertia are. After the inertial support by fast swing of the droop curve, the droop coefficient will recover to its original value with the voltage gradually stabilized.

IV. Design of Adaptive Droop Control Strategy

Within the limited swing range, the faster swing speed of the droop curve are, the larger supplied virtual inertia becomes. To balance the inertia response speed (i.e. improve the swing speed of the droop curve by a large K_2) and system stability, and to take K_{min} and K_{max} into account, the arc-tangent function for droop coefficient calculation is employed here. The design of this ADC strategy with controllable inertia is presented as follows.

A. Improved Adaptive Droop Coefficient Calculation

To realize adaptive swing of the droop curve within the allowable range, the arc-tangent function is adopted to improve the variable droop coefficient k given in (9). In view of the above analysis on Fig. 4, when P<0, the improved k considering K_{min} and K_{max} can be given as

$$k = \begin{cases} K_1 + \dfrac{K_{max} - K_1}{\pi/2}\arctan(K_2^{'}\dfrac{dV_{dc}}{dt}) & \dfrac{dV_{dc}}{dt} > 0 \\ K_1 + \dfrac{K_1 - K_{min}}{\pi/2}\arctan(K_2^{'}\dfrac{dV_{dc}}{dt}) & \dfrac{dV_{dc}}{dt} < 0 \end{cases}. \quad (14)$$

When P>0, the improved k can be given as

$$k = \begin{cases} K_1 + \dfrac{K_1 - K_{min}}{\pi/2}\arctan(K_2^{'}\dfrac{dV_{dc}}{dt}) & \dfrac{dV_{dc}}{dt} > 0 \\ K_1 + \dfrac{K_{max} - K_1}{\pi/2}\arctan(K_2^{'}\dfrac{dV_{dc}}{dt}) & \dfrac{dV_{dc}}{dt} < 0 \end{cases}. \quad (15)$$

Combining (14) and (15) and taking the sign of $K_2^{'}$ into account, the improved k can be given as

$$k = \begin{cases} K_1 + \dfrac{K_{max} - K_1}{\pi/2}\arctan(K_2^{'}\dfrac{dV_{dc}}{dt}) & K_2^{'}\dfrac{dV_{dc}}{dt} > 0 \\ K_1 + \dfrac{K_1 - K_{min}}{\pi/2}\arctan(K_2^{'}\dfrac{dV_{dc}}{dt}) & K_2^{'}\dfrac{dV_{dc}}{dt} < 0 \end{cases}. \quad (16)$$

In a practical control system, the detection of dV_{dc}/dt is sensitive to noise and harmonic interference. Considering practical implementation, a washout filter is adopted to achieve the transient voltage variation δV_{dc} instead of dV_{dc}/dt, and (16) can be modified as

$$k = \begin{cases} K_1 + \dfrac{K_{max} - K_1}{\pi/2}\arctan(K_2^{'}\delta V_{dc}) & K_2^{'}\delta V_{dc} > 0 \\ K_1 + \dfrac{K_1 - K_{min}}{\pi/2}\arctan(K_2^{'}\delta V_{dc}) & K_2^{'}\delta V_{dc} < 0 \end{cases}. \quad (17)$$

Fig. 5 shows the difference of the calculated droop coefficient by (9) and (16). As seen, the arc-tangent function has a larger slope initially which then reduces gradually. Thus, it is more sensitive to small values and can smoothly transit to the limits. As δV_{dc} is normally smaller than dV_{dc}/dt especially at the initial stage, the droop coefficient k calculated by arc-tangent function is more effective. Even for the initial small δV_{dc}, the k calculated by (17) can be relatively large, which implies that the swing speed of the droop curve is faster at the initial stage of disturbances. As δV_{dc} further increases, the droop coefficient k will smoothly move to the limits, which is favorable for ensuring voltage stability.

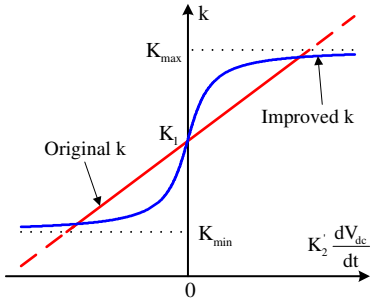

Fig. 5. Comparison between two calculation methods of the variable droop coefficient.

B. Real-Time Calculation of the Limits

The maximum swing amplitude of the droop curve depends on the limits of the droop coefficient. In order to make the most of the capability of a droop controlled converter in supplying virtual inertia, the real-time calculation of K_{max} should be executed.

Taking the operating points higher than the reference point (i.e. P<0) as an example, Fig. 6 compares different limits of k corresponding to three different steady state operating points A, B and C on the droop curve ①. For point A, when a power surplus occurs, the converter needs to reduce its power (i.e. further to the negative direction) and thus, the curve ① can swing anti-clockwise to curve ② at most with the output power decreasing from P_A to P_{min} to provide the maximum inertial support. The value of K_{max} when operating at point A is K_{A_max} and similarly, values of K_{max} for operating points B and C are K_{B_max} and K_{C_max}, respectively. If the value of K_{max} for point A is selected as K_{B_max}, curve ① can only be swung to curve ③ and the power decreases to P_A' rather than P_{min}. Since (P_A-P_{min}) is the maximum available power for the operating point A, the use of the limit K_{A_max} already ensures it being fully utilized. If K_{C_max} is selected, the curve ① will swing to curve ④, but no extra power can be output than that using K_{A_max} due to the converter power limit of P_{min}. However, the recovery progress becomes longer for the extra swing range, especially when P_A is close to P_{min}, which is detrimental to suppressing of the high frequency fluctuations. Hence, values of K_{max} for different operating points should be calculated in real time depending on the operating point prior to the transient. For the operating point being higher than the reference point and anti-clockwise swing, it can move to (P_{min}, V_{dc}) at most. Substituting (P_{min}, V_{dc}) into (1), K_{max} can be calculated as

$$K_{max} = \frac{-P_{min}}{V_{dc} - V_{dc}^*}. \tag{18}$$

The calculation method of K_{max} for operating points lower than the reference point is similar to that for higher operating points. Taking the position of operating points into account, K_{max} can be calculated as

$$K_{max} = \begin{cases} \dfrac{-P_{min}}{V_{dc} - V_{dc}^*} & V_{dc} > V_{dc}^* \\ \dfrac{P_{max}}{V_{dc}^* - V_{dc}} & V_{dc} < V_{dc}^* \end{cases}. \tag{19}$$

According to (19), the values of K_{max} varies with the moving of the operating point for fully utilizing the available power of the converter. For example, for a power surplus occurring at point A (V_A, P_A), the yielded point (V_A, P_{min}) by substituting (18) to (1) is exactly the maximum power point which point A can be shifted to. Thus, the real-time calculation of K_{max} can ensure the converter to provide appropriate inertial support under different operating points. Considering that the negative droop coefficient may cause stability issues, K_{min} in this paper is set to zero.

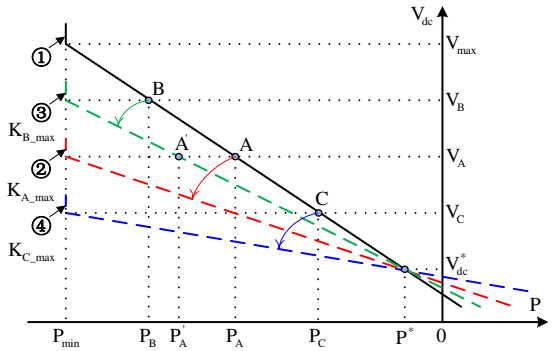

Fig. 6. Different values of K_{max} for different operating points.

C. Virtual Inertia Responses with Different Values of K_I

Defined as the steady-state droop coefficient, K_I reflects the primary voltage regulation ability of the converter and can be set accordingly though different K_I values can cause difference on the virtual inertia supplied by ADC.

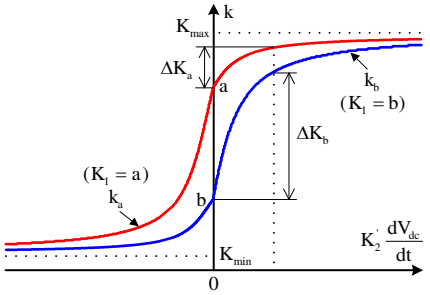

Fig. 7. Improved variable droop coefficients with different values of K_I.

Considering two different values of K_I, two improved droop coefficients are depicted in Fig. 7, where k_a and k_b correspond to the improved k with K_I=a and K_I=b (a>b) respectively. A power disturbance can lead to the variation of the improved k. Taking $K_2'dV_{dc}/dt$>0 for example, ΔK_a represents the variation of k_a while ΔK_b represents the variation of k_b. As ΔK_a is smaller than ΔK_b the swing amplitude of the droop curve with k_a is smaller than that with k_b. Thus it can be concluded that the virtual inertia supplied by ADC with a smaller K_I is larger. Similarly, the virtual inertia supplied by ADC with a larger K_I is larger when $K_2'dV_{dc}/dt$<0.

D. Controller Implementation

The proposed strategy utilizes fast swing of the droop curve to release/absorb energy quickly for emulating the inertial response. Thus it can be implemented to any droop controlled converters by changing the fixed droop coefficient with a variable one. For the DC grid shown in Fig. 1, the G-VSC and E-DCT normally adopt droop control for coordinated DC voltage regulation. Both of them can participate in virtual inertial support with ADC. However, to reduce the power fluctuations of AC grids or the repeat adjustments of the power supply, inertial response is preferably provided by the ESS.

However, if there is no ESS in the grid, the ADC has to be implemented in the G-VSC or other droop controlled converters. The block diagram of the proposed ADC is depicted in Fig. 8.

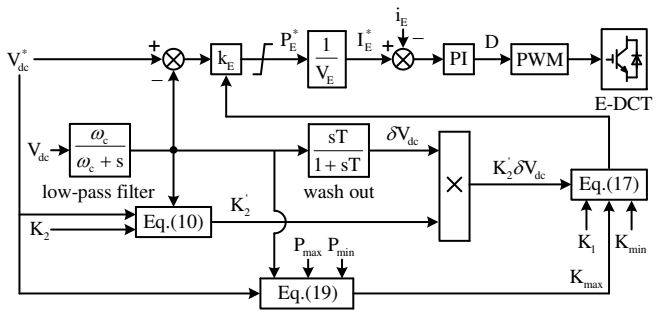

Fig. 8. Structure diagram of ADC for E-DCT.

In this paper, the proposed ADC is implemented on the E-DCT. When a power disturbance occurs, the BESS supplies auxiliary power to slow down the change rate of the DC bus voltage to improve the DC voltage quality. Due to the inertial energy generated by the E-DCT, the initial power fluctuations within the DC grid are mostly balanced by the BESS, which leads to reduced power fluctuations of the AC grid. Compared with the battery capacity, the supplied transient auxiliary power is relatively small. Therefore, the implementation of the proposed ADC on the E-DCT has little impact on the state of charge (SOC) of the BESS.

The droop curve is designed to swing at the initial stage of disturbances to improve the inertia of DC grids, and should not be affected by the steady voltage deviation. Thus, a washout filter is adopted to achieve the transient voltage variation δV_{dc}, and to reject steady state inputs. The time constant T of the washout filter is mainly determined by the designed cut-off frequency of the DC voltage variation.

Normally, the inertial response is provided during the initial tens to hundreds of milliseconds under disturbances. The power/current reference for this inertial support is generated by the fast swing of the droop curve, which depends on the voltage change rate rather than the bandwidth of the outer loop. Meanwhile, the bandwidth of the inner current loop of the DC-DC or AC-DC PWM converter is high enough to track the current reference variation in tens of milliseconds. After the inertial support period, the droop coefficient will recover to its origin constant value. Therefore, the bandwidth matching of the inner loop and outer loop can just follow the design principle of the conventional droop control, which makes the ADC easier to implement in droop controlled converters.

Parameters affecting ADC include K_1, K_2, K_{min} and K_{max}, as can be seen in (17). For a certain DC grid, the value K_1 is fixed to meet the requirements of the primary voltage regulation. As analyzed above, K_{min} is set to zero and K_{max} is calculated in real time according to the operation state. Therefore, the virtual inertia coefficient K_2 becomes the key controllable parameter to regulate the virtual inertia supplied by ADC. Equation (13) reveals that with a larger K_2, both the virtual capacitance and supplied virtual inertia become larger. However, excessively large inertia would result in increased power demand for the converter doing inertia control, and slowing down the voltage recovery process. Therefore, how much virtual inertia should be supplied to DC grid depends on the requirements to voltage quality and system stability.

V. Stability Analysis of The Proposed ADC Strategy

Voltage stability has drawn increased attentions in DC systems due to the high penetration of power electronic converters [26-27]. The virtual capacitance can improve the voltage quality of DC grids by suppressing voltage mutation rate. However, very large virtual capacitance may lead to system instability under a very low voltage change rate. In order to investigate the stability of the ADC, the small-signal model of a DC grid is established and its eigenvalue analysis is provided.

A. Small-signal modelling of the DC grid

1) Modelling of ESS terminal

The adaptive droop control is implemented on the ESS side converter E-DCT. Taking $V_{dc}<V_{dc}^*$ and $\delta V_{dc}<0$ as an example, the droop coefficient k_E for E-DCT can be expressed as

$$k_E = K_I + \frac{P_{max}/(V_{dc}^* - V_{dc}) - K_I}{\pi/2}\arctan(-K_2\delta V_{dc}) \qquad (20)$$

The duty cycle of the DC-DC converter is regulated by a PI controller to track the current reference generated by the ADC. The control diagram of the E-DCT including the low-pass and washout filters for small-signal stability analysis is shown in Fig. 9, where φ and θ are intermediate variables and ω_c is the cut-off frequency of the low-pass filter.

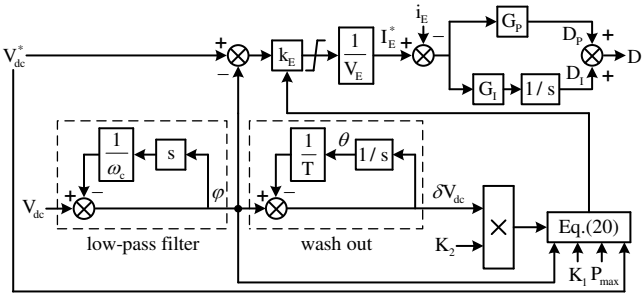

Fig. 9. Control diagram of the E-DCT for small-signal stability analysis.

The dynamic model of the E-DCT is given as

$$\begin{cases} L_E\dfrac{di_E}{dt} = V_E - (1 - D_P - D_I)V_{dc} \\ \dfrac{dD_I}{dt} = G_I\left(k_E\dfrac{V_{dc}^* - \varphi}{V_E} - i_E\right) \end{cases} \qquad (21)$$

where L_E is the inductance of the E-DCT. i_E and V_E are the current and voltage of the BESS. D_P and D_I are the duty cycles calculated from the proportional and integral control parts respectively. G_I is the integral coefficient of the PI controller. k_E is the droop coefficient of the ADC.

By using small signal approximation, (22) is linearized as

$$\frac{d\Delta\mathbf{x}_E}{dt} = \mathbf{A}_E\Delta\mathbf{x}_E + \mathbf{B}_E\Delta\mathbf{y} \qquad (22)$$

where $\Delta\mathbf{x}_E=[\Delta i_E \ \ \Delta D_I]^T$, $\Delta\mathbf{y}=[\Delta V_{dc} \ \ \Delta\varphi \ \ \Delta\theta]^T$. Matrixes $\mathbf{A}_E$ and $\mathbf{B}_E$ are given in Appendix.

2) Modelling of the DC grid

In order to simplify the small-signal analysis process, the following assumptions are given. The AC grid terminal is assumed as to be an infinite power source connected by an ideal

converter with droop control. The DC line impedance is neglected, and the PV terminal and wind turbine terminal are simply equivalent to power sources. All terminals are assumed to be connected to the same DC bus. Thus, according to Kirchhoff's current law (KCL), the dynamic model of the DC link is given as

$$C_{dc}\frac{dV_{dc}}{dt} = I_{dc\_G} + I_{dc\_E} + I_{dc\_RES} - I_{dc\_L} \tag{23}$$

where C_{dc} is the total capacitance of the common DC bus. I_{dc_G}, I_{dc_E}, I_{dc_RES} and I_{dc_L} are the respective DC side currents of the AC grid terminal, ESS terminal, RES terminal and load terminal, and can be further expressed as

$$\begin{cases} I_{dc\_G} = k_G(V_{dc}^* - V_{dc})/V_{dc} \\ I_{dc\_E} = (1 - D_P - D_I)i_E \\ I_{dc\_RES} = P_{RES}/V_{dc} \\ I_{dc\_L} = P_L/V_{dc} \end{cases} \tag{24}$$

where k_G is the droop coefficient of the G-VSC. P_{RES}、P_L are the RES power and load power respectively.

As shown in Fig. 9, the equations of φ and θ for small-signal analysis can be expressed as

$$\frac{d\varphi}{dt} = \omega_c(V_{dc} - \varphi)\,. \tag{25}$$

$$\frac{d\theta}{dt} = \varphi - \frac{\theta}{T}\,. \tag{26}$$

Taking V_{dc}, φ and θ as state variables, (23), (25) and (26) can be linearized as

$$\frac{d\Delta\mathbf{y}}{dt} = \mathbf{Y}_E\Delta\mathbf{x}_E + \mathbf{Y}_y\Delta\mathbf{y} \tag{27}$$

where matrixes $\mathbf{Y}_E$ and $\mathbf{Y}_y$ are given in Appendix.

According to (22) and (27), the linearized small-signal model of the DC grid is given as

$$\frac{d\Delta\mathbf{x}}{dt} = \mathbf{A}_{sys}\Delta\mathbf{x} \tag{28}$$

where $\Delta\mathbf{x}=[\Delta\mathbf{x}_E \ \ \Delta\mathbf{y}]^T$, and the complete matrix $\mathbf{A}_{sys}$ is given in Appendix.

B. Small-Signal Stability Analysis

The parameters and initial conditions of the DC grid are given in Table AI in Appendix. Based on the small-signal model expressed by (28), the trajectories of the eigenvalues with the virtual inertia coefficients K_2 varying from 50 to 5500 in step of 50 are shown in Fig. 10. In this case, the control parameters of ADC and load conditions are set as: f_c=200Hz, T=0.1s, G_P=2, G_I=50, P_L=25kW, P_{RES}=10kW. It can be seen that, with the increase of the virtual inertia coefficient K_2, the real parts of the eigenvalues approach to zero, and become positive for K_2>5200. Therefore, K_{2_max}=5200 is considered to be the upper limit of the variable droop coefficient in the system stable region under the above condition.

However, the load/DG power changes and control parameters variations may affect the system stability with ADC. Hence system stability using eigenvalue analysis with different load conditions and control parameters is further investigated to determine K_{2_max}. The upper limits of K_2 under different load/DG power and control parameters are given in Table I and Table II respectively. It can be seen that, to guarantee system stability, the maximum allowed K_2 (i.e. K_{2_max}) varies during load variation, and the increasing of T and G_I or the decreasing of f_c and G_p will also lead to reduced K_{2_max}. Among these results, the minimum K_{2_max} is 1700 within reasonable variations of the control parameters. Therefore, k_{2_max} is set to smaller than 1000 to ensure system stability while still providing adequate inertial support for the DC grid. Taking K_2 = 500 as an example, and the root locus with control parameters varying of f_c (50~1000Hz), T (0.01~0.5s), G_P (0.5~5) and G_I (5~150) are analyzed and shown in Figs. 11 (a)-(d) respectively. As can be seen, all the eigenvalues are on the left half-plane during the control parameters variation. Thus, the system stability can be guaranteed when a lower K_2 (e.g. K_2<1000) is adopted.

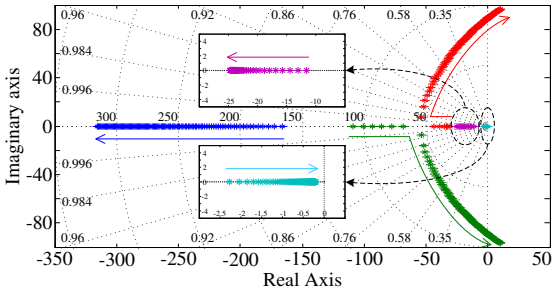

Fig. 10. The root locus of the ADC for the DC grid with different K_2.

TABLE I
Maximum Values of K_2 under Different Operating Conditions

P_L-P_{RES}	K_{2_max}	P_L-P_{RES}	K_{2_max}	P_L-P_{RES}	K_{2_max}
5kW	8950	15kW	5200	25kW	4900
10kW	6250	20kW	4850	30kW	5500

TABLE II
Maximum Values of K_2 under Different Control Parameters

f_c	K_{2_max}	T	K_{2_max}	G_P	K_{2_max}	G_I	K_{2_max}
50Hz	4150	0.01s	7650	0.5	1700	5	5500
100Hz	4500	0.05s	5150	1	3450	20	5250
200Hz	4850	0.1s	4850	2	4850	50	4850
500Hz	5150	0.2s	4700	3	5200	100	4250
1000Hz	5400	0.5s	4600	5	5450	150	3850

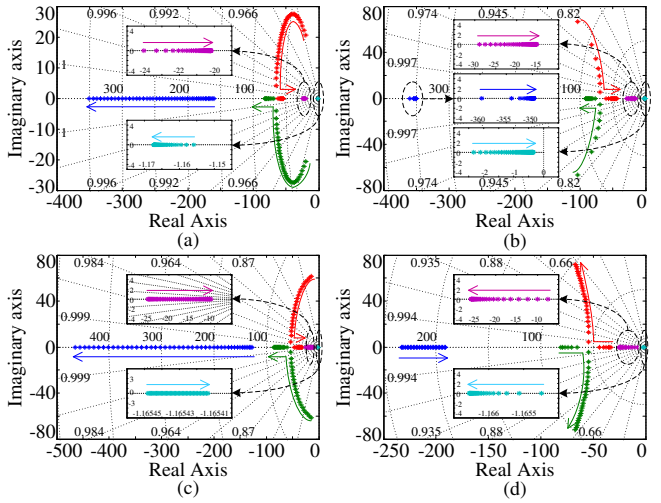

Fig. 11. The root locus with control parameters varying. (a) Varying of f_c. (b) Varying of T. (c) Varying of G_P. (d) Varying of G_I.

Under the premise of system stability, an adjustable virtual capacitance can be achieved by changing the droop coefficient in a large extent ($0<K_2<1000$), which can smooth and damp the higher frequency oscillations. Furthermore, the voltage change rate can be reduced effectively by the virtual capacitance. This would benefit the fault ride through (FRT) of the converters in DC grids under an abrupt disturbance, due to achieve a longer duration for FRT. Therefore, the proposed strategy improves the high frequency stability.

Since the inertial response by the proposed ADC is only emulated during the initial tens to hundreds of milliseconds of disturbances, it can effectively suppress voltage oscillations in the frequency range of several Hz to tens of Hz, which is called higher-frequency oscillations in this paper. For low frequency disturbances, some recent studies have shown that droop controlled converters may affect low-frequency stability of DC grids [27]. However, the virtual capacitance cannot be set too large considering the system stability. Moreover, in order to avoid the influence on the primary voltage regulation and power sharing of the droop control, the washout function is designed to filter out DC voltage deviation and low frequency voltage fluctuations below 1Hz. Therefore, the proposed ADC can be regarded as the conventional droop control under steady state and low frequency power/DC voltage variation.

VI. Hardware-in-the-Loop Testing Results

Experimental tests on a controller hardware in-the-loop simulation platform of a LV DC grid have been carried out to validate the proposed control strategy. The HIL platform shown in Fig. 12 is composed of a real-time digital simulator (an OP5600 RT-LAB), a TI's TMS320F28335 DSP board and a host computer. As illustrated in Fig. 12(a), control algorithms containing the proposed ADC for the BESS are deployed in DSP, while the control algorithms for other terminals and the real-time simulation model of a low-voltage DC grid are deployed in RT-LAB. The PWM pulses generated by DSP for E-DCT are fed to the pulse input port of RT-LAB through an optoelectronic isolation module, as shown in Fig. 12(b). The min-BNC interfaces of RT-LAB are connected with a DL850 wave recorder to display the test results. Table AI in Appendix lists the detailed parameters of the real-time simulation model illustrated in Fig. 12(a), where P_{WT}, P_L, P_B and P_G are the PMSG-based wind turbine output power, AC loads power, BESS power and AC grid power, respectively.

In this paper, the G-VSC and E-DCT are coordinated by voltage droop control and the proposed ADC is implemented on E-DCT. The control parameters for G-VSC and E-DCT are also listed in Table AI. Meanwhile, K_{min} is set to zero and K_{max} is calculated in real time, while different values of K_2 can be selected to acquire different virtual inertia responses. For the experimental results, positive P_G and P_B refer to the AC grid and BESS output power to the DC grid. k is the droop coefficient for E-DCT. P_R is the required power of the LV DC grid caused by the wind turbine and the AC loads.

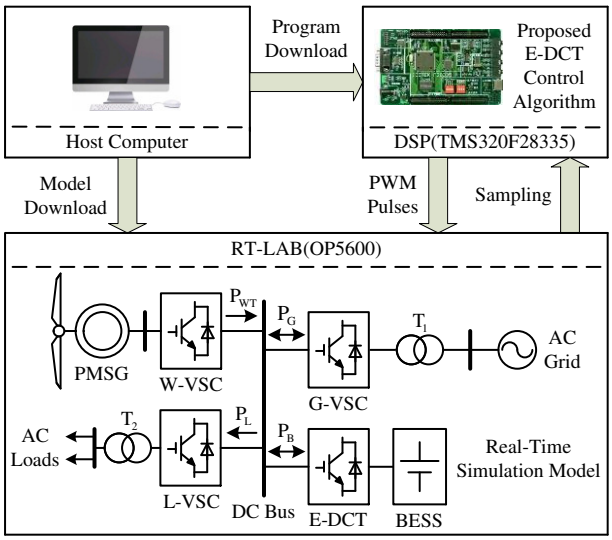

(a)

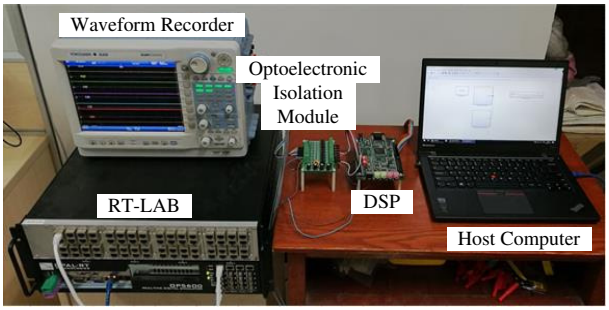

(b)

Fig. 12. HILS platform of a DC grid. (a) System design. (b) Experimental platform.

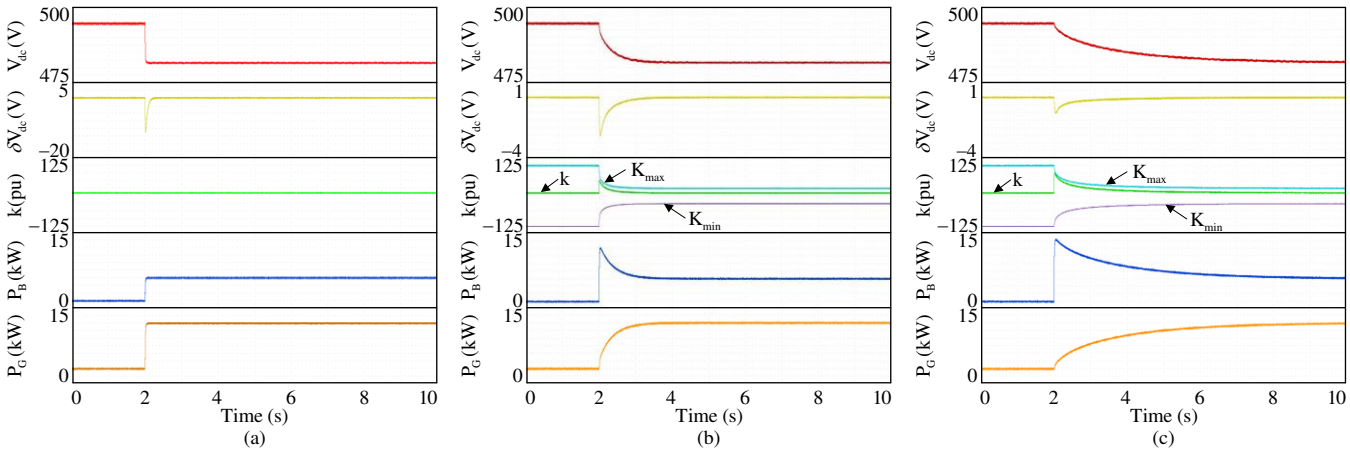

Fig. 13. Dynamic responses during sudden power increase. (a) Without virtual inertia control. (b) With ADC (K_2=500). (c) With ADC (K_2=3000).

A. Sudden Power Change Test

In order to verify the proposed ADC and analyze the impact caused by different values of K_2, tests under sudden power changes are performed firstly. In Fig. 13, the required power is increased from 4.5kW to 18kW, while in Fig. 14, the required power is decreased from 18kW to 4.5kW.

Fig. 13(a) shows the test results without virtual inertia control. At the beginning, the DC bus voltage V_{dc} is controlled around 495V by E-DCT and G-VSC. At 2s, the required power suddenly increases, and due to the small system inertia, V_{dc} quickly droops to 480V and a large voltage variation δV_{dc} of -11V can be observed. Based on the same condition, Fig. 13(b) shows the test results when the proposed ADC with K_2=500 is applied. As can be seen, the droop coefficient k for E-DCT varies with V_{dc} and the auxiliary power is supplied by the BESS to enhance the system inertia. After the sudden power increase, k is increased from 10pu to 50pu and P_B is increased to supply the auxiliary power of 6kW. As a result, a reduced δV_{dc} of −2.5V is observed. Due to the virtual inertia, the transient time of V_{dc} is prolonged, and the change of P_G is slowed down. To supply larger virtual inertia, ADC with K_2=3000 is applied and the test results are demonstrated in Fig. 13(c). When the required power suddenly increases, k is increased to 75pu and P_B is increased to supply a larger auxiliary power of 8kW. As a result, a smaller δV_{dc} of -1V is observed and the transient time is much prolonged. The comparison between Fig. 13(b) and Fig. 13(c) reveals that with a larger K_2, the virtual inertia supplied by ADC is larger.

Fig. 14 shows the test results under a sudden power decrease, and the measurement noise is added to the DC voltage signal to replicate practical conditions. As can be seen from the filtered voltage, i.e. $\bar{V}_{dc}$, the measurement noise is almost eliminated by the low-pass filter with a cut-off frequency of 200Hz. Thus, the δV_{dc} can still properly reflect the change rate of the DC voltage despite introducing the noise interference. From Fig. 13 and Fig. 14, it can be seen that the limits are calculated in real-time and k adaptively varies within the limits. Furthermore, the virtual inertia supplied by ADC can be regulated by adjusting the value of K_2, so different requirements for virtual inertia can be met.

B. Higher-frequency Random Power Fluctuations Test

To further illustrate the advantages of the proposed ADC, tests of higher-frequency random power fluctuations are carried out and the results are shown in Fig. 15. At the beginning, the required power P_R of the DC grid fluctuates between 4.5kW and 9kW. At 5s, a load of 9kW is switched on.

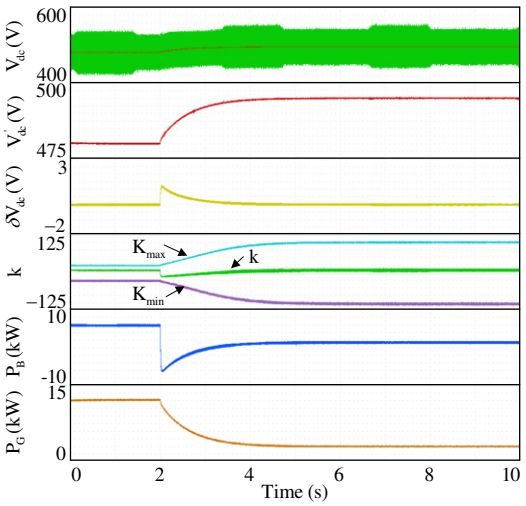

Fig. 14. Dynamic responses with ADC (K_2=500) during sudden power decrease while considering the measurement noise.

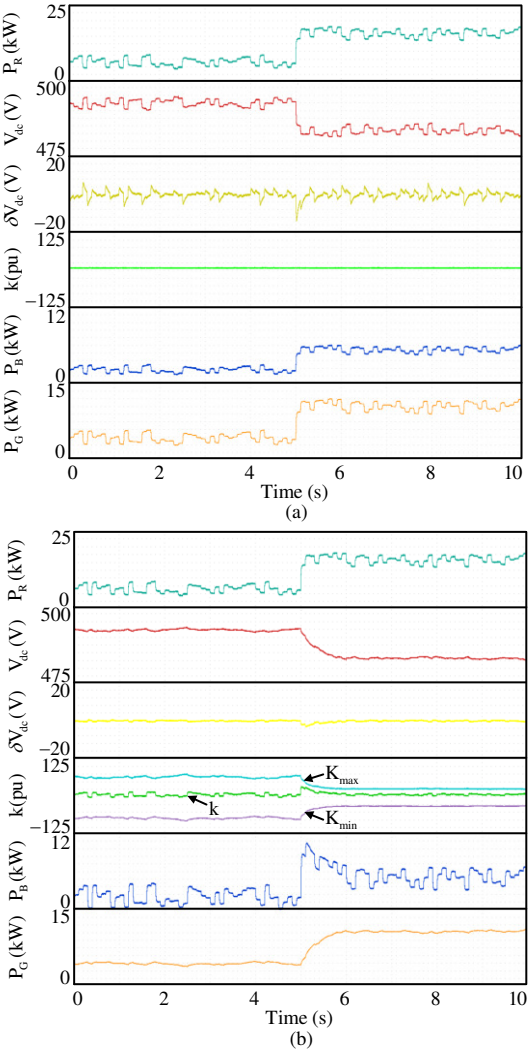

Fig. 15. Dynamic responses during random power fluctuations. (a) Without virtual inertia control. (b) With ADC.

Fig. 15(a) shows the system dynamic responses without virtual inertia control. Due to the lack of inherent inertia, V_{dc} changes significantly. Meanwhile, the power fluctuations within the DC grid are transmitted to the AC grid, which is not

desirable for the AC grid. Fig. 15(b) shows the test results when the proposed ADC with K_2=500 is applied. It can be seen that V_{dc} is significantly smoothed due to the virtual inertia. As the power fluctuations are mostly balanced by the BESS, a much smoother P_G is also observed. Auxiliary power is supplied by the BESS and the average value of P_B is almost the same as that in Fig. 15(a), so the implementation of ADC has little impact on the SOC of the BESS.

The virtual capacitance only suppresses voltage flicker and high frequency variation, without affecting the steady-state voltage deviation. Fig. 13 shows the reduction of the voltage change rate using the ADC in the event of the load step changes, which can help to reduce the voltage flicker. Fig. 15 shows the high frequency variations are suppressed, which can help to smooth the DC bus voltage and enhance voltage quality. The voltage deviation still exits due to droop control, but it can be further reduced and even restored to the rated value by the secondary voltage regulation. The results of this voltage recovery process are not given due to the secondary voltage regulation is not studied in this paper.

C. Coordination of Two Terminals with ADC

In this case, both the AC grid and ESS terminals adopt ADC to investigate their interaction with their virtual inertia coefficients set as K_{2G}=K_{2E}=500. In addition, the system performances under lower-frequency (0.2Hz) and higher-frequency (20Hz) oscillations caused by the load fluctuations are incorporated in the case studies. The HIL test results are shown in Fig. 16. As can be seen, the ADC can work properly for both oscillations, but the damping effect of the higher-frequency oscillation is obviously better than that of low-frequency oscillation. Due to both AC grid terminal and ESS terminal provide inertial responses, the power oscillations caused by the load variation are shared by them according to their capacity.

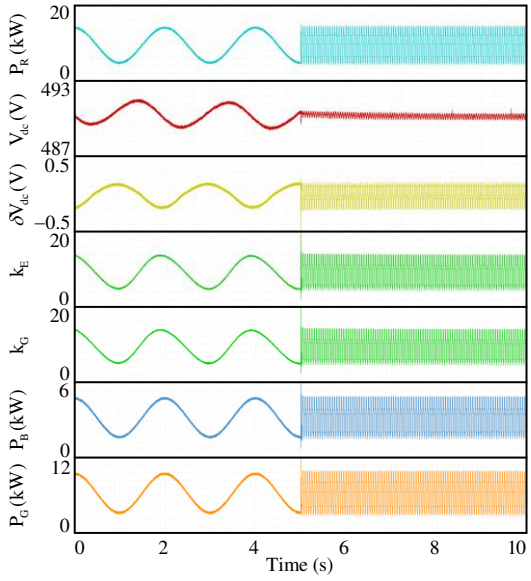

Fig. 16. Dynamic responses with multiple ADC during lower- and higher-frequency oscillations.

VII. Conclusion

Under the fixed droop control, the distinct unbalanced power added to the small capacitor at the initial stage of the disturbances can result in rapid changes of the DC voltage. This paper proposes an adaptive droop control strategy to increase the equivalent inertia of the DC grid. It can not only mitigate the mutation rate and fluctuations of the DC voltage and improve the power supply quality, but also has the following advantages.

(1) By simply replacing the fixed droop coefficient with the adaptive one, the ADC can be easily applied to droop controlled converters without adding any auxiliary controller or observer. The emulated virtual capacitance can be adjusted flexibly by changing the virtual inertia coefficient K_2, to meet the requirements of voltage quality while ensuring system stability.

(2) It can provide both inertial response and primary voltage regulation for the DC grid in an integrated controller. The ADC strategy can make the droop curve swing quickly during the initial stage of large disturbances to provide inertial support, and recover to the conventional droop control as the voltage gradually becomes stable. By introducing the arc-tangent function, the ADC properly swings the droop curve to achieve a larger inertia without causing system oscillation. Meanwhile, the real-time calculation of the limits ensures the ADC adaptable to different operation states within the allowed range.

(3) It has negligible effect on power sharing among the converters in the DC grid and power quality in the AC grid. The converter with ADC only provides additional transient power support, and has constant droop coefficient during the subsequent power distribution by the system primary and secondary regulation. Considering that power fluctuations are not desirable for the AC grid, the proposed ADC implemented on the BESS can also smooth the AC grid power exchange to improve the power quality of the AC grid.

Appendix

The complete matrixes of the DC grid small-signal model are given below.

$$\mathbf{A}_{sys}=\begin{bmatrix}\mathbf{A}_E & \mathbf{B}_E\\ \mathbf{Y}_E & \mathbf{Y}_y\end{bmatrix}$$

$$\mathbf{A}_E=\begin{bmatrix}-\dfrac{G_P V_{dc0}}{L_E} & \dfrac{V_{dc0}}{L_E}\\ -G_I & 0\end{bmatrix}$$

$$\mathbf{B}_E=\begin{bmatrix}\dfrac{-1+D_0}{L_E} & \dfrac{\mu G_P V_{dc0}}{L_E} & \dfrac{\lambda G_P V_{dc0}}{L_E}\\ 0 & \mu G_I & \lambda G_I\end{bmatrix}$$

$$\mathbf{Y}_E=\begin{bmatrix}\dfrac{1-D_0+G_P i_{E0}}{C_{dc}} & -\dfrac{i_{E0}}{C_{dc}}\\ 0 & 0\\ 0 & 0\end{bmatrix}$$

$$\mathbf{Y}_y = \begin{bmatrix} -\dfrac{k_G V_{dc}^* + P_{RES} - P_L}{C_{dc} V_{dc0}^2} & -\dfrac{\mu G_P i_{E0}}{C_{dc}} & -\dfrac{\lambda G_P i_{E0}}{C_{dc}} \\ \omega_c & -\omega_c & 0 \\ 0 & 1 & -\dfrac{1}{T} \end{bmatrix}$$

where the coefficients μ and λ in the matrixes are expressed as

$$\mu = \frac{V_{dc}^* - \varphi_0}{V_E}\alpha - \frac{k_{E0}}{V_E}$$

$$\lambda = \frac{V_{dc}^* - \varphi_0}{V_E}\beta$$

$$\alpha = \frac{2}{\pi}\frac{1}{1+K_2^2(\varphi_0-\theta_0/T)^2}(K_1+\frac{P_{max}}{\varphi_0-V_{dc}^*})K_2 - \frac{2}{\pi}\frac{P_{max}}{(\varphi_0-V_{dc}^*)^2}\arctan(K_2\varphi_0-\frac{K_2}{T}\theta_0)$$

$$\beta = -\frac{2}{\pi}\frac{1}{1+K_2^2(\varphi_0-\theta_0/T)^2}(K_1+\frac{P_{max}}{\varphi_0-V_{dc}^*})\frac{K_2}{T}.$$

The nominal parameters of the simulated DC grid and the initial condition for its small-signal analysis are given below.

TABLE AI
SYSTEM PARAMETERS AND INITIAL VALUES OF THE DC GRID

Items	Parameters & Values
DC Bus Voltage	V_{dcN}=500V
AC Grid	S_N= 33kVA, V_{acN}=380V, L_s=0.05pu T1: k_{T1}=380/220 , L_{T1}=0.05pu
G-VSC (Two-level VSC)	P_N=30kW, V_N=220V, C=2000μF Droop controller: V_{dc}^*=500V, P_{min}=−30kW, P_{max}=30kW, k_G=10 Current controller (p.u.): k_p=1 k_I=50
BESS	300V/200A•h
E-DCT (Bi-direction DC-DC converter)	P_N=15kW, V_{iN}=300V, V_{oN}=500V, L=1mH, C=390μF ADC: V_{dc}^*=500V, P_{max}=15kW, K_I=10
PMSG	P_N=20kW, v_N=12m/s
AC Loads	P_N=30kW
Initial Condition	k_{E0}=10, φ_0=V_{dc0}, θ_0=T·V_{dc0}, i_{E0}=K_I(V_{dc}^*-V_{dc0})/V_E, D_0=1-V_E/V_{dc0} (V_{dc0} is related to P_{RES} and P_L)

REFERENCES

[1] M. Ranjram, and P. W. Lehn, "A multiport power-flow controller for DC transmission grids," IEEE Trans. Power Del., vol. 31, no. 1, pp. 389-396, Feb. 2016.

[2] K. A. Saleh, A. Hooshyar and E. F. El-Saadany, "Hybrid passive-overcurrent relay for detection of faults in low-voltage DC Microgrids," IEEE Trans. Smart Grid, vol. 8, no. 3, pp. 1129-1138, May 2017.

[3] L. Xu and D. Chen, "Control and operation of a DC microgrid with variable generation and energy storage," IEEE Trans. Power Del., vol. 26, no. 4, pp. 2513-2522, Oct. 2011.

[4] R. Ahmadi, and M. Ferdowsi, "Improving the performance of a line regulating converter in a converter-dominated DC microgrid system," IEEE Trans. Smart Grid, vol. 5, no. 5, pp. 2553-2563, Sep. 2014.

[5] B. Liu, F. Zhuo, Y. Zhu, and H. Yi, "System operation and energy management of a renewable energy-based DC micro-grid for high penetration depth application," IEEE Trans. Smart Grid, vol. 6, no. 3, pp. 1147-1155, May 2015.

[6] N. Chaudhuri, and B. Chaudhuri, "Adaptive droop control for effective power sharing in multi-terminal DC Microgrids," IEEE Trans. Power Syst., vol. 28, no. 1, pp. 21-29, Feb. 2013.

[7] C. Gavriluta, I. Candela, A. Luna, A. Gomez-Exposito, and P. Rodriguez, "Hierarchical control of HV-MTDC systems with droop-based primary and OPF-based secondary," IEEE Trans. Smart Grid., vol. 6, no. 3, pp. 1502-1510, May 2015.

[8] P.-K. Keung, P. Li, H. Banakar, and B. T. Ooi, "Kinetic energy of wind-turbine generators for system frequency support," IEEE Trans. Power Syst., vol. 24, no. 1, pp. 279- 287, Feb. 2009.

[9] X. Liu, P. Wang, and P. C. Loh, "A hybrid AC/DC microgrid and its coordination control," IEEE Trans. Smart Grid, vol. 2, no. 2, pp. 278-286, Jun. 2011.

[10] H. P. Beck and R. Hesse, "Virtual synchronous machine" in 9th International Conference on Electrical Power Quality and Utilisation, Barcelona, Spain, 2007, pp. 1-6.

[11] Q.-C. Zhong and G. Weiss, "Synchronverters: Inverters that mimic synchronous generators," IEEE Trans. Ind. Electron., vol. 58, no. 4, pp. 1259-1267, Apr. 2011.

[12] Q.-C. Zhong, P.-L. Nguyen, Z. Ma, and W. Sheng, "Self-synchronized synchronverters: Inverters without a dedicated synchronization unit," IEEE Trans. Power Electron., vol. 29, no. 2, pp. 617-630, Feb. 2014.

[13] Y. Wang, J. Meng, X. Zhang, and L. X, "Control of PMSG-based wind turbines for system inertial response and power oscillation damping," IEEE Trans. Sustain. Energy, vol. 6, no. 2, pp. 565-574, Apr. 2015.

[14] B. Liu, F. Zhuo, and X. Bao, "Control method of the transient compensation process of a hybrid energy storage system based on battery and ultra-capacitor in micro-grid," in Proc. IEEE ISIE Conf, May 2012, pp. 1325-1329.

[15] D. Wu, F. Tang, T. Dragicevic, J. M. Guerrero, and J. C. Vasquez, "Coordinated control based on bus-signaling and virtual inertia for islanded DC microgrids," IEEE Trans. Smart Grid, vol. 6, no. 6, pp. 2627-2638, Nov. 2015.

[16] X. Zhu, J. Cai, Q. Yan, J. Chen, and X. Wang, "Virtual inertia control of wind-battery-based islanded DC micro-grid," in Proc. IET RPG Conf., Oct. 2015, pp. 1-6.

[17] W. Wu, Y. Chen, A. Luo, L. Zhou, X. Zhou, L. Yang, Y. Dong, and J. M. Guerrero, "A virtual inertia control strategy for DC microgrids analogized with virtual synchronous machines," IEEE Trans. Ind. Electron., vol. 64, no. 7, pp. 6005-6016, Jul. 2017.

[18] E. Prieto-Araujo, A. Egea-Alvarez, S. Fekriasl, and O. Gomis-Bellmunt, "DC voltage droop control design for multiterminal HVDC systems considering AC and DC grid dynamics," IEEE Trans. Power Del., vol. 31, no. 2, pp. 575-585, Apr. 2016.

[19] Y. Gu, X. Xiang, W. Li and X. He, "Mode-adaptive decentralized control for renewable DC microgrid with enhanced reliability and flexibility," IEEE Trans. Power Electron., vol. 29, no. 9, pp. 5072-5080, Sep. 2014.

[20] K. Rouzbehi, A. Miranian, J. I. Candela, A. Luna and P. Rodriguez, "A generalized voltage droop strategy for control of multiterminal DC Microgrids," IEEE. Ind. App., vol. 51, no. 1, pp. 607-618, Jan./Feb. 2015.

[21] R. Eriksson, J. Beerten, M. Ghandhari, and R. Belmans, "Optimizing DC voltage droop control settings for AC/DC system interactions," IEEE Trans. Power Del., vol. 29, no. 1, pp. 362-369, Feb. 2014.

[22] Y. Xia, W. Wei, Y. Peng, P. Yang and M. Yu, "Decentralized coordination control for parallel bidirectional power converters in a Grid-Connected DC Microgrid," IEEE Trans. Smart Grid , vol. PP, no. 99, pp.1-12, Jul. 2017.

[23] Y. Xia, W. Wei, M. Yu, Y. Peng and J. Tang, "Decentralized multi-time scale power control for a hybrid AC/DC microgrid with multiple subgrids," IEEE Trans. Power Electronics, vol. PP, no. 99, pp.1-12, Jun. 2017.

[24] Y. Li, L. He, F. Liu, C. Li, Y. Cao and M. Shahidehpour, "Flexible voltage control strategy considering distributed energy storages for DC distribution network," IEEE Trans. on Smart Grid, vol. PP, no. 99, pp. 1-12, Jul. 2017.

[25] X. Li, L. Guo, S. Zhang, C. Wang, Y. Li, A. Chen, and Y. Feng, "Observer-based DC voltage droop and current feed-forward control of a DC microgrid," IEEE Trans. Smart Grid, vol. PP, no. 99, pp. 1-9, Mar. 2017.

[26] M. Zhang, Y. Li, F. Liu, L. Luo, Y. Cao and M. Shahidehpour, "Voltage stability analysis and sliding mode control method for rectifier in DC systems with constant power loads," IEEE Journal of Emerging and Selected Topics in Power Electronics, vol. 5, no. 4, pp. 1621-1630, Dec. 2017.

[27] N. Rashidirad, M. Hamzeh, K. Sheshyekani, and E. Afjei, "A Simplified Equivalent Model for the Analysis of Low-Frequency Stability of Multi-Bus DC Microgrids,"IEEE Trans. Smart Grid, vol. pp, no. 99, pp. 1-1, May 2017.